

Chapter 2

Review: Prediction of Respiratory Motion

Radiation therapy is a cancer treatment method that employs high-energy radiation beams to destroy cancer cells by damaging the ability of these cells to reproduce [1]. In external beam radiotherapy (EBRT), specific parts of the patient's body are exposed to the radiation emanating from a treatment machine [1–3]. The X-ray beams have to penetrate other body tissues to reach the target area during treatment process. This leads to unnecessary irradiation of healthy tissues around the tumors. Accordingly, prediction of respiratory motion is a very critical issue in EBRT. Radiation technologies can consist of two major approaches: (1) tools for measuring target position during radiotherapy [4–9], where patient-specific treatment parameters including acquisition of respiratory patterns, treatment simulation, and target area planning are determined for treatment preparation, and (2) tracking-based delivery systems [10–14], where the patient is placed under the linear accelerator and radiation is delivered using real-time tracking methods under free breathing conditions.

2.1 Tools for Measuring Target Position During Radiotherapy

Measuring target position for treatment planning in radiotherapy is heavily dependent on image processing and patient-specific interpretation methods for medical data and images [15–25]. There exist several measuring tools for the target position. Once the target is identified, it is easy to track this defined target in most imaging modalities [26]. A number of medical imaging, such as radiographs, fluoroscopy, computed tomography (CT), magnetic resonance imaging (MRI), and optical imaging can provide real-time information in company with outstanding visualization to improve the treatment results during beam delivery [23]. It is difficult to detect the target directly in images. The fiducial markers are often employed to act as surrogates for optical signal tracking.

2.1.1 Radiographs

Radiographs (referred to as plain X-rays) are photographic images produced by the activity of X-ray or nuclear radiation to view a non-uniformed physical object. The rays may penetrate the human body through the different density and structure of the object. The rays that pass through are recorded behind the object with a detector which can display the different density and structure of the body. Generally, radiographies are generated by X-ray beams, whereas in nuclear medicine gamma rays are involved [27]. Radiographs are unceasingly used and employed as a major tool to detect and measure the target position [28].

2.1.2 Fiducial Markers

Fiducial markers located around the tumor position are often employed to act as surrogates for optical signal tracking, to synchronize the internal and external breathing motion signals, and to provide real-time information during beam delivery [26, 29–34]. In real-time tumor tracking, multiple implanted fiducial markers are detected as surrogate on the images of fluoroscopy systems for accurate tumor location, but their use can be limited due to the risk of pneumothorax during marker implantation [30, 33, 34]. External fiducial markers are also attached on the patient's chest for respiratory gated radiotherapy, where they can be used to correlate internal breathing motion with external optical signal based on the infrared tracking system [2, 26, 35].

2.1.3 Fluoroscopy

Fluoroscopy is a method for obtaining real-time moving images of deep body structures using fluoroscope [26]. A patient is placed between an X-ray tube and fluorescent screen during fluoroscopic procedures. Modern fluoroscopes are associated with an image intensifier and video camera so that they can display a continuous series of images with maximum 25–30 images per second [36]. Fluoroscopy is often used not only to watch the digestive track but also to track moving organs during therapeutic procedures [28, 31, 37].

2.1.4 Computed Tomography

Computed tomography (CT) [4, 23, 28, 29] is a specialized X-ray imaging method employing a series of individual small X-ray sensors with computer processing.

Here, medical data come together with multiple angles, and a computer treats this information to generate an image (referred to as “cut”). The vision of body images is similar to the vision of a sliced bread loaf. CT images are widely used for diagnostic purposes, especially for diagnosing a variety of tumors including lung, pancreas, liver, and other thoracic and abdominal tumors, because using CT images can not only validate that tumors exist, but they also determine tumor position and size to provide clear images for radiation treatment planning [5, 8, 40]. X-ray computed tomography (CT) including computed axial tomography (CAT) and cone beam CT (CBCT) uses rotating X-ray equipment with a digital computer to produce a clear medical image for all types of tissues [41].

2.1.5 Magnetic Resonance Imaging

Magnetic resonance imaging (MRI) is a medical imaging method that uses the property of nuclear magnetic resonance, instead of radiative delivery to the patient to visualize the internal organs and tissues for diagnosis and therapy planning. MRI aligns the protons in the water atoms within the patient using a strong magnetic field. Then, a very sensitive radio antenna detects the resonance signal of the protons that are activated by the electromagnetic pulse of the scanner [27]. In MRI, the picture of body images looks similar to a “cut” in CT. MRI provides good contrast between the different soft tissues compared with X-ray CT, so that it can create a highly detailed image of the scanned body structures in the soft tissues [42]. The integrated and hybrid MRI modalities also proposed to improve the treatment outcome [23, 42].

2.1.6 Optical Imaging

Optical imaging is a non-invasive imaging method that takes photographs of biological tissues or organs using visible, ultraviolet, and infrared wavelengths for clinical diagnosis [43]. Unlike X-ray photons that penetrate the entire biological tissue, optical photons interact with biological tissue medium by the property of absorption and elastic scattering [44]. Advanced optical imaging modalities have been recently developed, so they can provide cost-effective and much higher resolution images than current CT and MRI images [43]. Optical imaging system consisting of infrared cameras and external markers can also provide accurate position of target tracking during the treatment process in real-time [45].

2.2 Tracking-Based Delivery Systems

Conventional radiotherapy systems used linear accelerators with gantry mechanism to delivery the radiation beam to the targeting areas [46]. Due to the breathing-induced tumor motion, breath-holds and gating methods are used to reduce underdosing of tumor parts and overdose to surrounding critical parts [47]. Multileaf collimator (MLC)-based and couch-based tracking methods also have been developed for real-time tumor tracking under free breathing conditions [10, 12, 31, 47–52].

2.2.1 Linear Accelerator

Linear accelerator (Linac) is the medical device to generate the therapeutic beam for EBRT treatment [46]. Linacs accelerate electrons by high-voltage electric fields, and then let these electrons collide with source target to produce high-energy X-ray beams. Linacs may be equipped with specialized blocks or a multileaf collimator (MLC) in the head of machine to conform fields to the shape of the patient's tumor. Finally, the customized beam can be delivered by a gantry mechanism (such as robotic arms) to specific parts of the patient to destroy the malignant tumors [9, 46].

For example, CyberKnife is a well-known image-guided radiosurgery system for Linac applications [53]. The two main elements of the system are the linear particle accelerator to generate radiation for treatment, and a robotic arm to allow the radiation to be delivered at any target area of the body with six degrees of freedom [28]. Advanced image guidance technology, e.g., X-ray sources to generate orthogonal X-ray images, is used to detect the bony landmarks location, implanted fiducials or soft tissue tumors. IR tracking system synchronized with the tumor motion can reduce safety margins for respiratory gating or breath-hold techniques, as shown in Fig. 2.1 [2, 46, 54].

The simple treatment process includes planning, repetition of verification and targeting, and treatment delivery. In the planning process, X-ray image scanning and advanced treatment planning are prepared. In the repetition of verification and targeting process, the image-guided radiosurgery system verifies clinical tumor location. If any variation is detected in the tumor position, the robotic arm is replaced according to the tumor movement based on a frame. In the treatment process, the sophisticated radiation beam for radiosurgery is delivered to the tumor [53]. The synchrony respiratory tracking system is widely used to continuously synchronize the delivery of radiation beam to the motion of the tumor for real-time tumor tracking [12, 54–61].

There are many radiation therapy equipments to support prediction of respiratory motion with advanced radiotherapy technologies [62]. The outline of all the radiotherapy systems is out of scope in this study. Among many radiation therapy

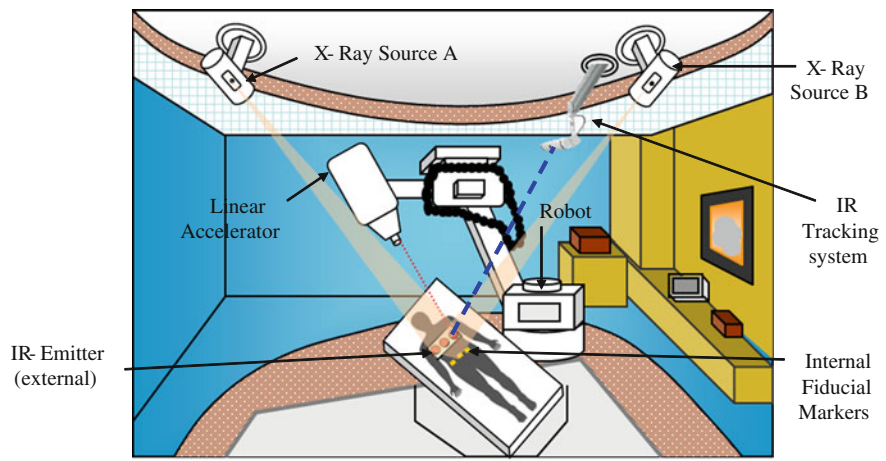


Fig. 2.1 CyberKnife system. X-ray source with low energy is used to detect soft tissue tumors or implanted fiducial markers during the treatment. IR tracking system synchronized with the tumor motion can reduce safety margins for respiratory gating or breath-hold techniques [46, 53]

systems, some radiotherapy equipments are widely used for the management of respiratory motion [26], such as CyberKnife robotic treatment device (Accuray, Inc., Sunnyvale, CA) [53, 54], Real-time position management system (RPM system, Varian Medical, Palo Alto, CA) [63, 64], Real-time tumor-tracking system (RTRT, Hokkaido University) [65–67], Elekta system (Elekta Ltd, Stockholm, Sweden) [10, 48, 68, 69], and Siemens Radiation Oncology system (Siemens AG, Munich, Germany) [70, 71]. Therefore, we describe five main radiotherapy equipments as shown in Table 2.1.

2.2.2 Multileaf Collimator

Multileaf collimator (MLC) is a sophisticated system for radiation therapy dose delivery, made up of separate leaves that can move independently in and out of a particle beam path to form a desired field shape as shown in Fig. 2.2.

Table 2.1 Instrumentations for radiation therapy

Radiotherapy systems	Development
CyberKnife robotic treatment [53]	Accuray, Inc., Sunnyvale, CA
Varian real-time position management system [63, 64]	RPM system, Varian Medical, Palo Alto, CA
Real-time tumor-tracking system [65, 66]	RTRT system, Mitsubishi Electronics Co., Ltd., Tokyo
Elekta system [10, 48, 68, 69]	Elekta Ltd, Stockholm, Sweden
Siemens radiation oncology system [70, 71]	Siemens AG, Munich, Germany

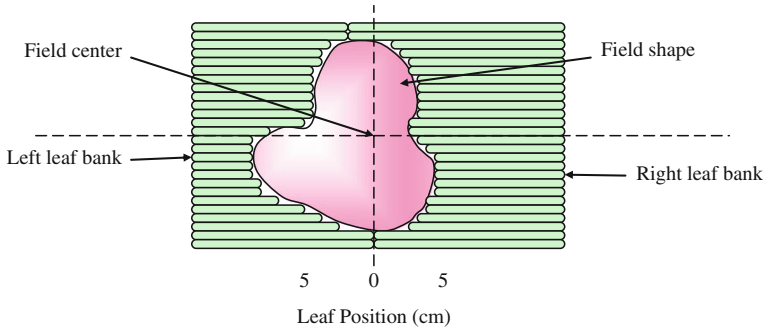


Fig. 2.2 A multileaf collimator (MLC) with a desired field shape. MLC is made up of separate leaves that can move independently in and out of a particular beam path to form a desired filed shape

The advantage of MLC is that it can simply change an individual leaf for the field shape with controlling remote computer and save treatment preparation time by eliminating clinician's entering the treatment room [49].

Sawant et al. proposed an integrated system by combining an independent position monitoring system and an intensity-modulated radiotherapy (IMRT) delivery system based on dynamic MLC (DMLC). In [12], they investigated two important parameters, i.e., system latency and geometric accuracy. To reduce the system latency, the tracking algorithm used a modified linear adaptive filter with continuous megavoltage X-ray images of three implemented transponders at approximately seven frames per second. The geometric accuracy was calculated by comparing the aperture center of each image frame with the target motion trajectories. MLC-based tracking method may increase the treatment accuracy and decrease the treatment time compared to breath-holds and gating methods [50, 51].

2.2.3 Robotic Couch

A robotic couch can be used to compensate for breathing-induced tumor motion with extra degree of precision for patients in real time [10, 48]. For the couch-based tracking method, a robotic couch system consists of stereoscopic infrared cameras and the couch system moves in response to any changes in angle and position of organ motion detected by the cameras during treatment delivery [31, 47].

Figure 2.3 shows HexaPOD robotic couch with six degrees of freedom. The couch system consists of top (moving) frame linked with a fixed base frame using independent mechanical legs. Here the top platform is defined by six independent position-orientation variables—coordinates $(x, y, z, \alpha, \beta, \gamma)$ [10, 52]. The commercially available robotic couches can arrange the patient position according to the treatment procedure with highly accurate level; however, they lack compensation for the respiratory and cardiac motion [10, 48].

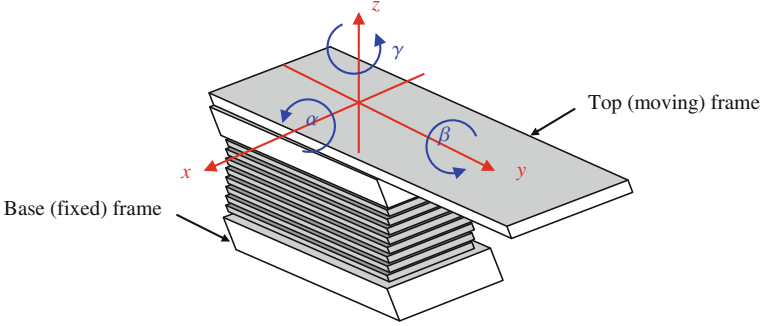


Fig. 2.3 External view of robotic couch with six degrees of freedom. The couch system consists of top (moving) frame linked with a fixed base frame using independent mechanical legs. Here the top platform is defined by six independent position-orientation variables—coordinates ($x, y, z, \alpha, \beta, \gamma$) [10]

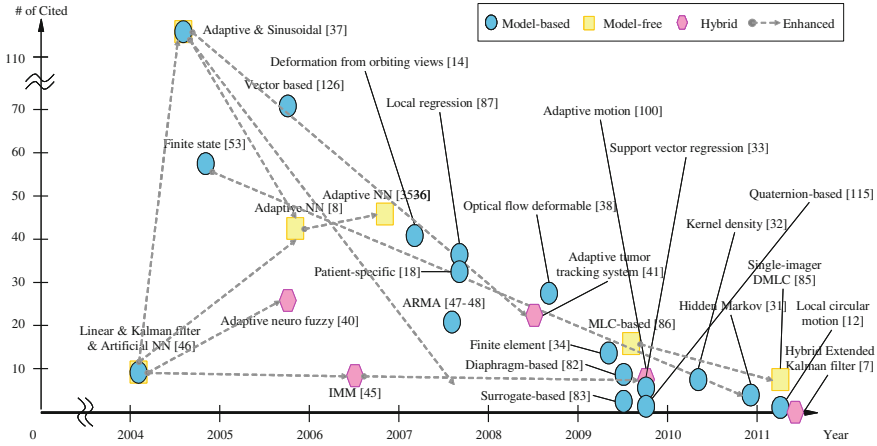


Fig. 2.4 Variable prediction algorithms for respiratory motion. This figure shows the key studies, which have more than 30 references in the last 10 years, representing to the salient algorithms covered

2.3 Prediction Algorithms for Respiratory Motion

A number of prediction methods for respiratory motion have been investigated based on surrogate markers and tomography images [5, 16, 38, 55, 56, 72–78]. The previous methods can be categorized into three approaches: (1) *model-based* approach [38, 55, 56, 73, 75, 77] which uses a specific biomechanical or mathematical model for respiratory motion functions or models; (2) *model-free* approach [57, 68, 74, 75, 79] heuristic learning algorithms that are trained based on the observed respiratory patterns; (3) *hybrid* approach [80, 81], which uses united

methods to combine more than two methods, resulting in outperforming the previous solitary method. These three approaches are described in the following Sects. 2.3.1, 2.3.2, and 2.3.3, respectively. Figure 2.4 shows the key studies, which have more than 30 references in the last 10 years, representing the salient algorithms covered.

2.3.1 Model-Based Prediction Algorithms

Generally, *model-based* methods include (1) linear prediction [73–75, 82], (2) Kalman filter [72, 73, 75, 81–84], (3) sinusoidal model [74, 82], (4) finite state model [73, 78, 82], (5) autoregressive moving average model [76, 77, 82], (6) support vector machine [7, 56, 61, 82, 85–87], and (7) hidden Markov model [73, 78]. Especially, linear approaches and Kalman filters are widely used for the fundamental prediction approach of respiratory motion among a variety of investigated methods [5, 16, 38, 39, 55, 56, 73–78, 88–92].

2.3.1.1 Linear Prediction

A linear prediction is a mathematical system operation where future output values are estimated as a linear function of previous values and predictor coefficients, as follows [75, 82]:

$$\hat{x}(t) = a_0 + a_1x(t-1) + \cdots + a_nx(t-n) = \sum_{i=0}^n a_ix(t-i), \quad (2.1)$$

where $\hat{x}(t)$ is the predicted value or position at time t .

The predicted value is a linear combination of previous observations $x(t-n)$ and predictor coefficients a_n that are not changing over time, as shown in Fig. 2.5. In a linear prediction, it is a significant task to solve a linear equation to find out the coefficients a_n that can minimize the mean squared error between the predicted values and previous values [75]. The linear model is widely used in the early stage to compare the prediction performance with other models, e.g. neural network prediction and Kalman filtering [73, 75]. Sharp et al. revealed that the root mean squared error (RMSE) for the prediction accuracy is around 2.2 mm with 200 ms latency [75]. The limitation of this model is that it is not robust to some changes from one linear state to another [73]. This model can be enhanced into nonlinear (sinusoidal) and adaptive models as shown in Fig. 2.4 [74].

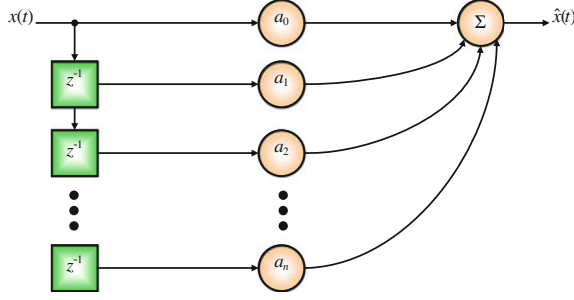


Fig. 2.5 Linear predictor with tapped-delay line. The predicted value is a linear combination of previous observations $x(t - n)$ and predictor coefficients a_n that are not changing over time

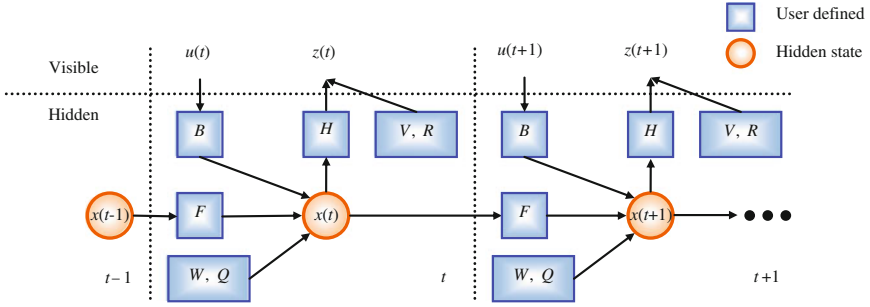


Fig. 2.6 Roles of the variables in the Kalman filter. $u(t)$ is an n -dimensional known vector, and $z(t)$ is a measurement vector. The next state is calculated based on the dynamic equation, such as $x(t+1) = Fx(t) + Bu(t) + V$. Here, V and W are process noise and measurement noise with covariance R and Q

2.3.1.2 Kalman Filter

The Kalman filter (KF) is one of the most commonly used prediction methods in real-time filtering technologies [72, 73, 75, 81–83]. KF provides a recursive solution to minimize mean square error within the class of linear estimators, where linear process and measurement equations to predict a tumor motion can be expressed as follows [84]:

$$\hat{x}(t) = Fx(t-1) + Bu(t-1) + W, \quad z(t) = H\hat{x}(t) + V, \quad (2.2)$$

where we denote the state transition matrix as F , the control-input matrix as B , and the measurement matrix as H . $u(t)$ is an n -dimensional known vector, and $z(t)$ is a measurement vector. The random variables W and V represent the process and measurement noise with the property of the zero-mean white Gaussian noise with covariance, $E[W(t)W(t)^T] = R(t)$ and $E[V(t)V(t)^T] = Q(t)$, respectively. The matrices F , B , W , H , and V are assumed known and possibly time-varying (Fig. 2.6).

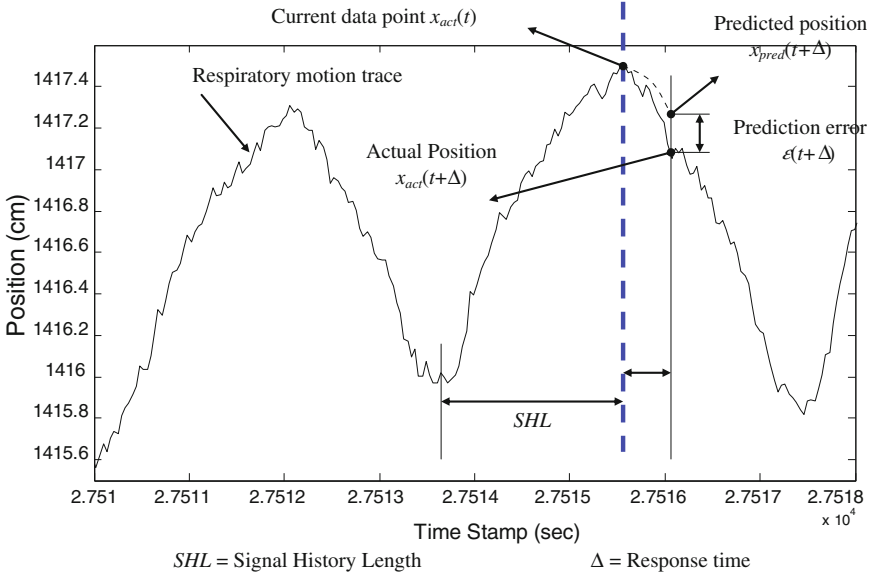


Fig. 2.7 Explanation of signal history length (SHL) explanation of SHL, response time (Δ) and prediction error with respect to the current data point. Let $x(t)$ denote the actual respiratory motion curve at time t after SHL. The predicted position $x_{pred}(t + \Delta)$ can be calculated based on the sinusoidal curve fit model over SHL

In KF, the predicted position $\hat{x}(t)$ can be derived from the previous state $x(t - 1)$ and the current measurement $z(t)$ [82, 84]. Sharp et al. showed that RMSE for the prediction accuracy is around 2.5 mm with 200 ms latency [75]. Because of state update process with new data, KF is effective for linear dynamic systems, but prediction accuracy is degraded when breathing patterns change from one linear state to another [73]. KF was enhanced to interactive multiple model (IMM) filter with constant velocity (CV) and constant acceleration (CA) based on KF by Putra et al. in Fig. 2.4 [81, 83]. Hong et al. also suggested the first-order extended Kalman filter (EKF) can be used to process and update the state estimate [72].

2.3.1.3 Sinusoidal Model

Regular respiratory motion shows a continuous sinusoidal pattern with respect to the time sequence. This sinusoidal curve can be adjusted to respiratory motion over signal history length (SHL). We show Fig. 2.7 to clarify the ideas of SHL, response time (Δ), and prediction error for a single point of respiratory motion trace. Let $x(t)$ denote the actual respiratory motion curve at time t after SHL. Vedam et al. represented a sinusoidal wave model to estimate the predicted position for a given response time (Δ), as follows [74]:

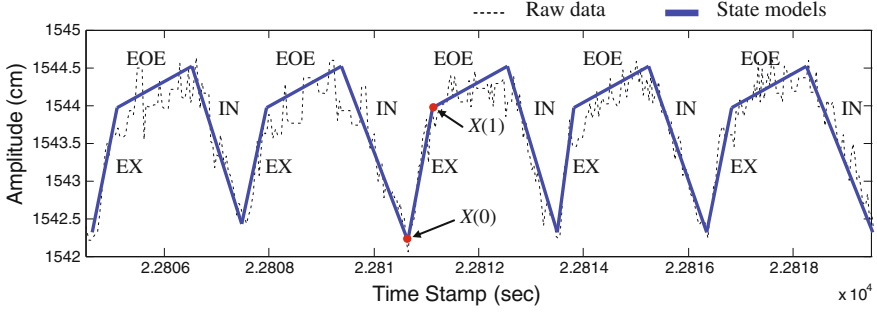


Fig. 2.8 Finite state model with regular breathing cycles. The breathing motion patterns are modeled with irregular (IRR), exhale (EX), end-to-exhale (EOE), and inhale (IN) breathing states [78]. State transitions are initiated by the velocity of tumor motion with two vector points $X(t_0)$ and $X(t_1)$

$$x_{pred}(t + \Delta) = x_{act}(t) + [x_{SHL}(t + \Delta) - x_{SHL}(t)], \quad (2.3)$$

where $x_{SHL}(t)$ is a fitted sinusoidal curve including SHL, given by $x_{SHL}(t) = A \sin(Bt + C) + D$ with time sequences from t -SHL to t ($t > SHL$, and A , B , C , and D are the parameters of sinusoidal waveform model) [74].

Vedam et al. evaluated that the prediction error with 200 ms latency is less than 2 mm. This model also has a limitation with 1D prediction and the prediction accuracy degrades with long latency [74, 82].

2.3.1.4 Finite State Model

The breathing motion can be analyzed based on its natural understanding of breathing states [78]. In finite state model (FSM), a regular respiratory motion is subdivided into three states—exhale (EX), end-to-exhale (EOE), and inhale (IN), as shown in Fig. 2.8 [78, 82]. The other motions are categorized as irregular breathing (IRR) except the above three states in this approach. Wu et al. represented the finite state automation for the transition from one state to another [78]. Line segments for finite states in Fig. 2.8 are determined by the velocity of tumor motion and the average amplitude for two connected directed line segments. Let $X(t) = \{x_0, x_1, \dots, x_n\}$ as an n -dimensional vector point at time t . The length of a directed line segment from $X(t_0)$ to $X(t_1)$ is expressed as follows:

$$\|\overrightarrow{X_0 X_1}\| = \sqrt{\sum_{i=1}^n (x_{1i} - x_{0i})^2}. \quad (2.4)$$

The velocity of tumor motion is calculated with two vector points ($X(t_0)$ and $X(t_1)$), as follows:

$$v(t_0 \rightarrow t_1) = \frac{\|\overrightarrow{X_0 X_1}\|}{t_0 - t_1}. \quad (2.5)$$

This method provides not only a statistically quantitative analysis of motion characteristics, but also good prediction results, i.e., average RMS error less than 1 mm. However, the study on FSM is restricted to a one dimension model. This method was enhanced into a three dimension version with hidden Markov model by Kalet et al. [73].

2.3.1.5 Autoregressive Moving Average Model

Autoregressive moving average (ARMA) model is a mathematical generalization of the linear model with time series data and signal noise, and widely used to predict motion patterns of a time series from past values [76, 77, 82]. ARMA consists of two models: (1) an autoregressive (AR) model represented by a weighted sum of the present and past positions with a polynomial order p , i.e., $\varphi_1 x(t-1) + \dots + \varphi_p x(t-p)$, and (2) a moving average (MA) model represented by a weighted sum of the present and past signal noise with a polynomial order q , i.e., $\theta_1 \varepsilon(t-1) + \dots + \theta_q \varepsilon(t-q)$ [76, 82]. The mathematical notation ARMA (p, q) with polynomial orders of p AR and q MA is expressed as follows [77]:

$$\hat{x}(t) = \varepsilon(t) + \sum_{i=1}^p \phi_i x(t-i) + \sum_{i=1}^q \theta_i \varepsilon(t-i), \quad (2.6)$$

where we define ϕ_i as the parameter of the AR model, and θ_i as the parameter of MA model, respectively. The error terms $\varepsilon(t)$ are the white noise assuming to be independent and identically distributed random variables. The order of ARMA model was built on the combination of p and q with maximizing the Akaike information criterion. There is no limitation with sampling data and processing time to select the orders p and q . However, McCall et al. demonstrated that up to ARMA (4, 4) models were preferred and the ARMA (2, 1) models achieved the optimized mean prediction errors over all the latency investigated [77]. Ren et al. also showed that the standard deviation of the position is below 2.6 mm with prediction in contrast with 4.6 mm without prediction [76].

2.3.1.6 Support Vector Machine

Support vector machines (SVMs) are supervised learning methods that are widely used for classification and regression analysis [56, 61, 85–87]. For medicine applications, they have been used to predict lung radiation-induced pneumonitis from patient variables and compute the future location of tumors from patient geometry and clinical variables [7, 82, 87]. Let define $G(x)$ as an unknown

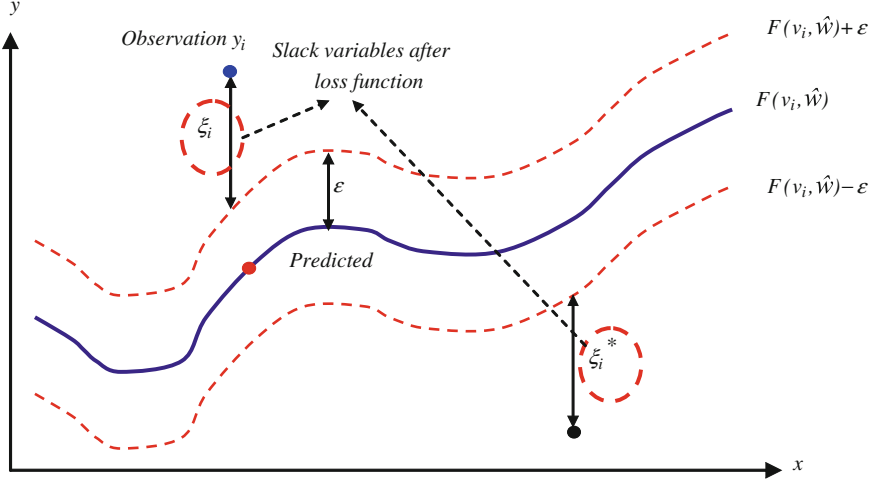


Fig. 2.9 Parameters for support vector regression. Let define ϵ as a user defined threshold, and $v_i (i = 1, \dots, N)$ as N training samples. The loss function is defined using the threshold ϵ , such as if the observation is within the threshold, the loss is zero; otherwise, the loss is the amount of the difference between the predicted value and the threshold ($|y_i - F(v_i, \hat{w})| - \epsilon$)

function (truth) with d -dimensional input vector $x = [x_1, \dots, x_d]$, $F(x, \hat{w})$ as a function with estimation \hat{w} derived from minimizing a measurement error between $G(x)$ and $F(x, \hat{w})$. Using N training samples $v_i, i = 1, \dots, N$, the primal objective function with a loss function $L(\cdot)$ can be expressed, as follows [86]:

$$C \sum_{i=1}^N L[y_i - F(v_i, \hat{w})] + \|\hat{w}\|^2, \quad (2.7)$$

where, C is a control value to adjust a balance, y_j is the observation of $G(x)$ in the presence of noise. The function $L(\cdot)$ is a general loss function with user defined threshold ϵ , as shown in Fig. 2.9, i.e., if the observation is within the threshold ($|y_i - F(x_i, \hat{w})| < \epsilon$), the loss is zero; otherwise, the loss is the amount of the difference between the predicted value and the threshold ϵ , such as ($|y_i - F(x_i, \hat{w})| - \epsilon$) [85, 86]. Based on the loss function and the threshold, the objective function (2.7) is calculated by solving the optimization problem as follows:

$$\min_w C \left(\sum_{i=1}^N \xi_i^* + \sum_{i=1}^N \xi_i \right) + \frac{1}{2} (w^t w), \quad (2.8)$$

where ξ_i and ξ_i^* are slack variables as shown in Fig. 2.9. A control value C is used to adjust the balance between the error term and the weight concentration [86]. This optimization problem can be resolved by the Lagrangian relaxation using Lagrangian multipliers [85, 86].

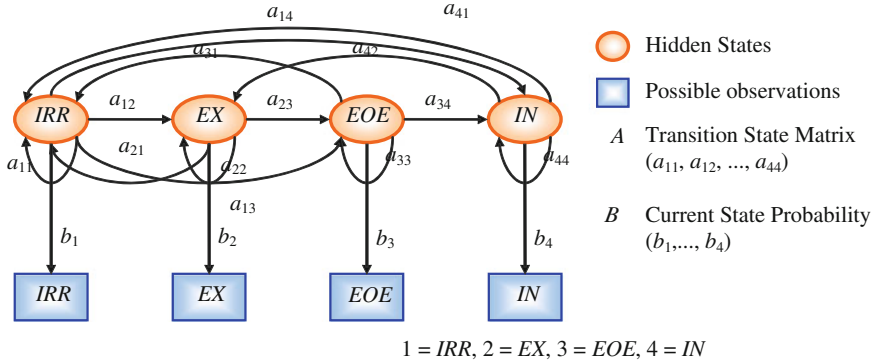


Fig. 2.10 Probabilistic predictive model based on Hidden Markov model. The transition state probability a_{ij} from the present state i to the next state j summarized to unity, such that $\sum_j a_{ij} = 1$. The current state probability is calculated based on the time percent in a particular breathing cycle, such that $\sum_i b_i(t) = 1$

Riaz et al. implemented an SVM regression model to predict the future location of the tumor, and showed that the prediction performance of RMSE was less than 2 mm at 1000 ms latency [56]. However, the prediction error using machine learning increased monotonically with fewer data points in the training samples. In addition, initial model parameters at the beginning of a treatment required to be adjusted due to the pattern change of a patient respiration [56, 61]. That resulted in the high computational complexity and the slow response time of prediction [85].

2.3.1.7 Hidden Markov Model

A hidden Markov model (HMM) is a statistical probability model with invisible state transition, where states are not directly visible, but a particular state can generate one of observations based on observation probabilities [73]. In [73], state distributions of the finite state model (FSM)—irregular (IRR), exhale (EX), end-to-exhale (EOE), and inhale (IN) in three dimension [78]—are used to create HMM with transition state matrix (A) and current state probability (B) based on the fractional time of a particular breathing cycle. Each state is determined by the previous state, and is distinguished with velocity (v_i). We denote a_{ij} as the transition state probability from the present state i to the next state j , such that $\sum_j a_{ij} = 1$, b_i as the current state probability to be calculated based on the time percent in a particular breathing cycle, such that $\sum_i b_i(t) = 1$, as shown in Fig. 2.10 [73].

The transition probability in Fig. 2.10 assumes that there is no possibility of physical movement from EOE state to EX state, or from IN state to EOE state, and so on. To eliminate these transition elements, the transition state matrix can be expressed by replacing those values with zero, as follows:

Table 2.2 Model-based prediction algorithms of respiratory motion

Methods	Prediction error and evaluation metrics	Features (system)
Linear predictor [75]	Around 2.2 mm with 200 ms latency, RMSE	RMSE at 10 Hz (RTRT)
Kalman filter [75]	Around 2.5 mm with 200 ms latency, RMSE	RMSE at 10 Hz (RTRT)
Sinusoidal model [74]	Less than 2 mm with 200 ms latency, standard deviation	1D prediction (RPM)
Finite state model [78]	Less than 1.5 mm, RMSE	Three line segments (EX-EOE-IN) (RTRT)
Vector model based on tidal volume and airflow [92]	0.28–1.17 mm	Standard deviation (digital spirometer)
Patient-specific model using PCA [5]	Around 2–3 mm, standard deviation	Respiration-correlated CT (RPM)
Autoregressive moving average model [20, 71]	0.8 mm with 200 ms latency, standard deviation	Image rate: 1.25–10 Hz (RTRT, RPM)
Deformation from orbiting views [16]	2.5 mm (LR), 1.7 mm (SI), standard deviation	Cone-beam CT
Local regression method [90]	2.5 mm	Local weighted regression, RMSE (RPM)
Optical flow deformable algorithm [39]	1.9 mm	Standard deviation (Philips CT scanner)
Finite element method [38]	3 mm (end expiration–end inspiration), 2 mm (end expiration–mid respiration)	Patient-specific models (Philips CT scanner)
Surrogate-based method [89]	2.2–2.4 mm (carina), 3.7–3.9 mm (diaphragm)	Standard deviation (RPM)
Diaphragm-based method [88]	2.1 mm	Standard deviation (RPM)
Support vector regression method [56]	Less than 2 mm at 1000 ms latency, RMSE	30 Hz sample frequency (CyberKnife)
Quaternion-based method [91]	2.5 (standard deviation)	Phantom matching error (PME)
Hidden Markov model [73]	1.88 ms at 200 ms latency, RMSE	Various latency: 33–1000 ms (RTRT)
Kernel density estimation-based [55]	1.08 mm at 160 ms, 2.01 mm at 570 ms, RMSE	Multidimensional prediction (CyberKnife)
Local circular motion model [72]	Less than 0.2 (nRMSE) at 200 ms normalized RMSE	First-order EKF, 5, 10, 15, 20 Hz (RPM)

$$A(t) = \begin{pmatrix} a_{11} & a_{12} & a_{13} & a_{14} \\ a_{21} & a_{22} & a_{23} & 0 \\ a_{31} & 0 & a_{33} & a_{34} \\ a_{41} & a_{42} & 0 & a_{44} \end{pmatrix}, \quad (2.9)$$

To predict motion with HMM, the future position of an observation is calculated using the velocity parameter (v_i) based on FSM,

$$\hat{x}(t) = x(t-1) + \sum_l v_l \tau, \quad (2.10)$$

where variable τ ($=1/RT$) consists of the sampling rate (R) and the estimated cycle period (T), and l represents the dimension. Kalet et al. showed that the RMSEs of ideal HMM and linear prediction are 1.88 and 2.27 mm with 200 ms latency. The limitation of this model is that the implemented algorithm is based on stochastic process so that the prediction results can be different even with the same data [73]. We summarized the prediction accuracy and a representative feature for each method of the *model-based* approach, as shown in Table 2.2.

2.3.2 Model-Free Prediction Algorithms

Model-free heuristic learning algorithms, exemplified by linear adaptive filters and neural networks variables, can be used for the respiratory prediction for compensating for the impaired breathing signal with a variety of breathing patterns [57, 74, 79, 93]. These heuristic learning algorithms can adjust their coefficients/weights or configurations to reproduce newly arrived breathing signals without a priori models of signal history [93]. In this chapter, we will explain two representative learning algorithms and adaptive systems for tumor prediction including (1) adaptive filters [57, 74, 79, 93–95], and (2) artificial neural network [57, 75, 79, 82, 93].

2.3.2.1 Adaptive Filters

An adaptive filter is a self-adaptive system that can adjust its coefficient values over time according to an optimization process incurred by an error signal, such as least mean squares (LMS) and recursive least squares (RLS) algorithms [96]. The adaptive filter depicted in Fig. 2.11 shows the basic adaptive filtering process for prediction.

The predicted position $\hat{x}(t)$ can be expressed by a vector of previous respiratory motion $x(t-i)$ and a vector of filter coefficients $w_i(t)$, as follows:

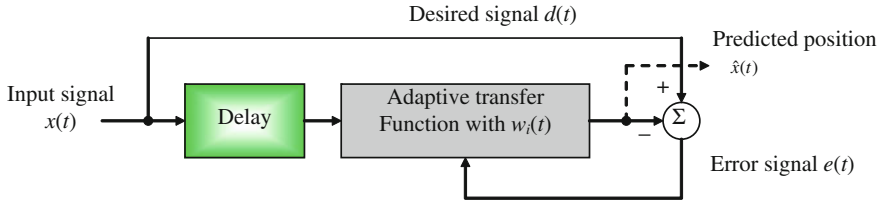


Fig. 2.11 Basic adaptive filtering process for prediction. The predicted position is calculated using the combination of previous respiratory motion $x(t - i)$ multiplied by its coefficient values $w_i(t)$. Here the coefficient values are time-variable according to an optimization process incurred by an error signal $e(t)$

$$\hat{x}(t) = \sum_{i=1}^n w_i(t)x(t - i), \quad (2.11)$$

where filter coefficients change over time. Adaptive filters were widely used to predict the tumor motion [57, 74, 79, 93, 95]. Vedam et al. proved that adaptive filter models have the prediction accuracy with less than 2 mm and outperform sinusoidal models [74]. Although the adaptive filter has a limitation with 1D prediction, it is extended into multi-dimensional adaptive filter [56]. Adaptive models can also be adjusted to update the weights of neural networks to improve the prediction accuracy [57, 79, 94].

2.3.2.2 Artificial Neural Network

An artificial neural network (ANN), commonly called neural network (NN), is a mathematical or computational function technique that is inspired by the

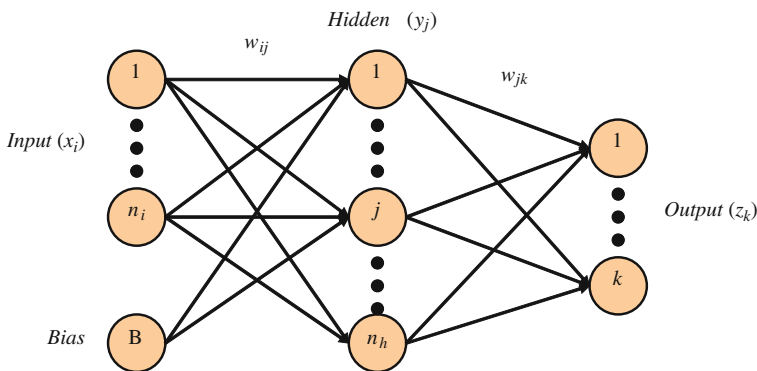


Fig. 2.12 An artificial neural network with bias input and one hidden layer. The network consists of input, hidden, and output layers interconnected with directed weights (w), where we denote w_{ij} as the input-to-hidden layer weights at the hidden neuron j and w_{jk} as the hidden-to-output layer weights at the output neuron k

biological neuron process [75]. A neural network consists of input, hidden, and output layers interconnected with directed weights (w), where we denote w_{ij} as the input-to-hidden layer weights at the hidden neuron j and w_{jk} as the hidden-to-output layer weights at the output neuron k , as shown in Fig. 2.12 [75, 82].

In Fig. 2.12, the input layer is a sequence history of breathing motions (n_i) with 3D positions. In the hidden layer, the intermediate value (y_j) is calculated with the history of breathing motions ($3n_i$) and bias unit using the nonlinear activation function, as follows [75]:

$$y_j = \frac{1}{1 + \exp\left(-\sum_{i=1}^{3n_i+1} w_{ij}x_i\right)}, \quad (2.12)$$

where we denote x_i as input values, and y_i as hidden values, respectively. The additional input unit (bias) is used to bias the linear portion of the computation. The practical prediction of respiratory motion is calculated with hidden values in the output neuron (z_k), as follows:

$$z_k = \sum_{j=1}^{n_h} w_{jk}y_j, \quad (2.13)$$

where output values z_k denote predictions of breathing motions, and neural weights (w_{ij} and w_{jk}) in the network are generally resolved by numeric optimization. Sharp et al. showed that the RMSE of NN predictor is less than 2 mm with low latency (33 ms) [75]. But they only considered the form of stationary prediction.

For the adaptive filter training, Isaksson et al. used a feed-forward neural network with two input neurons and one output neuron using the least mean square scheme [93]. Here, the external markers were used as surrogates to predict the tumor motion. This two-layer feed-forward neural network was used for predicting irregular breathing pattern by Murphy et al. as well [57, 79, 82]. The network was trained by a signal history from the beginning of the patient data record using back-propagation algorithm, and kept updating the network weights with new test data samples to adjust newly arrived breathing signals [57, 79]. This adaptive filter showed much better prediction error than stationary filter, e.g., RMSE of 0.5–0.7 mm for the most predictable cases and of 1.4–1.7 mm for the hardest cases with 200 ms latency [57].

Table 2.3 Model-free prediction algorithms of respiratory motion

Methods	Prediction error and evaluation metrics	Features (system)
Adaptive filter [74]	Less than 2 mm with 200 ms latency, standard deviation	1D prediction (RPM)
Artificial neural networks [75]	Around 2.5 mm with 200 ms latency, RMSE	RMSE at 10 Hz (RTRT)
Adaptive neural network [57, 79, 93]	1.4–1.7 mm with 200 ms latency, normalized RMSE	30 Hz sample frequency (CyberKnife)

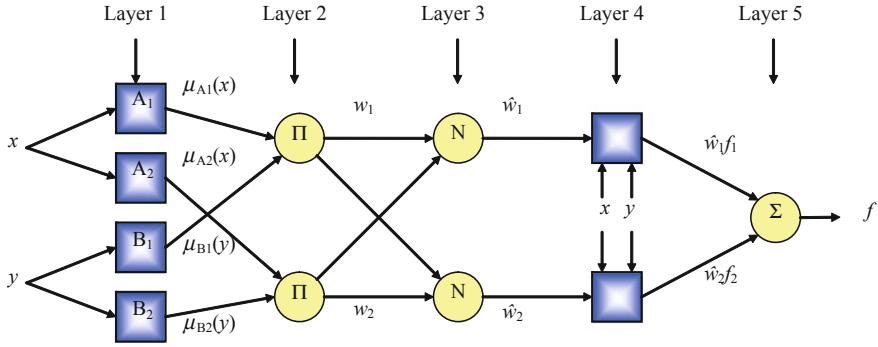


Fig. 2.13 Adaptive neuro fuzzy inference system with the total five layers. Based on the incoming elements (x and y), this system is composed with two layers of adaptive nodes (layers 1 and 4) and three layers of fixed nodes (layers 2, 3, and 5). The layer 1 is characterized by a membership function $\mu(\cdot)$ that assigns each incoming element to a value between 0 and 1. Layer 4 is trained by a least squares method

We summarized the prediction accuracy and a representative feature for each method of the *model-free* approach, as shown in Table 2.3.

2.3.3 Hybrid Prediction Algorithms

Hybrid prediction algorithms used united methods to combine more than two methods or approaches to obtain outstanding results, compared to a previous solitary method. This method includes (1) adaptive neuro-fuzzy interference system (ANFIS) [80, 97], (2) hybrid model with adaptive filter and nonlinear model (Adaptive Tumor Tracking System) [68, 98], and (3) interacting multiple model (IMM) filter [72, 81, 83].

2.3.3.1 Adaptive Neuro-Fuzzy Inference System

An adaptive neuro-fuzzy inference system (ANFIS) is a hybrid intelligent system with combining both learning capabilities of a neural network and fuzzy logic reasoning, to find a specific model in association with input breathing motion and target prediction. The proposed neuro-fuzzy model ANFIS in [80] is a multilayer neural network-based fuzzy system in combination with two layers of adaptive nodes (layer 1 and 4) and three layers of fixed nodes (layer 2, 3, and 5), as shown in Fig. 2.13 [80].

The first layer is distinguished by a fuzzy set (A_1, A_2, B_1, B_2) that is expressed by a membership function to assign each incoming element to a membership value between 0 and 1, as the following equation:

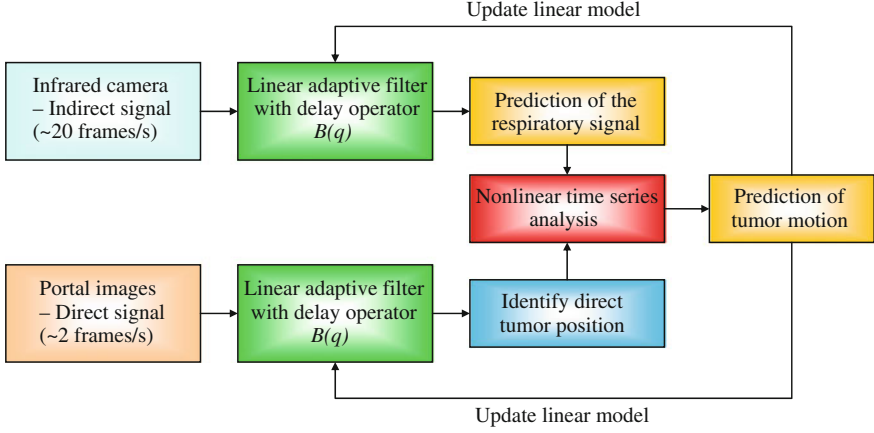


Fig. 2.14 Adaptive tumor tracking system with two independent signals. The tumor position is directly visualized and located by the acquired portal image (direct signal) using a tumor tracking algorithm without internal fiducial markers [68, 99]. Infrared camera signals (indirect signal) are used to predict respiratory signals using the adaptive filter, and these respiratory signals are correlated with the portal image to predict the tumor motion [98]

$$\mu_U(I; a_i, b_i, c_i) = \frac{1}{1 + \left| \frac{I - c_i}{a_i} \right| 2b_i}, \quad A, B \in U, \quad x, y \in I, \quad i = 1, 2, \quad (2.14)$$

where $I(x$ and $y)$ are incoming elements, and three parameters (a_i, b_i, c_i) (referred to as premise parameters) are continuously updated by training samples using a gradient descent method [80, 97]. Each node in the second layer is a fixed node, characterized by the product (Π) of all the incoming signals, such as $w_i = \mu_{A_i}(x) \cdot \mu_{B_i}(y)$, $i = 1, 2$. Each node in the third layer is a fixed node, characterized by the normalized ratio (N), such as $\hat{w}_i = w_i / (w_1 + w_2)$, $i = 1, 2$. Each node in the fourth layer is an adaptive node with a node function, such as $\hat{w}_i f_i = (p_i x + q_i y + r_i)$, $i = 1, 2$, where the parameter set (p_i, q_i, r_i) (referred to as consequent parameters) are trained by a least squares method. The single node in the last layer calculates the overall output by aggregating all incoming signals, such as $f = \sum_i \hat{w}_i f_i$, $i = 1, 2$. Kakar et al. validated that the prediction accuracy (RMSE) of respiratory motion for breast cancer patients was 0.628 mm with coached breathing and 1.798 mm with free breathing. This method required simpler and fewer remodeling decorations to implement its nonlinear ability in comparison to neural networks. However, for other conditions, exemplified by lung patients and respiration monitoring using spirometry or abdominal straps, it should associate the breathing signal with the target motion [80].

2.3.3.2 Hybrid Model with Adaptive Filter and Nonlinear Model

To compensate breathing tumor motion in the lung, an adaptive tumor-tracking system (ATTS) was proposed by Ma et al. with an adaptive filter and a nonlinear method [98]. Instead of only one signal, this adaptive system used two independent signals to detect the lung tumor motion during irradiation: (1) direct signal, i.e., imaging of irradiated region using megavoltage imaging of the treatment beam [99], and (2) indirect signal, i.e., optical marker with an infrared camera, as shown in Fig. 2.14 [68, 98]. The tumor position is directly visualized and located by the acquired portal image (direct signal) using a tumor tracking algorithm without internal fiducial markers [99]. Infrared camera signals (indirect signal) are used to predict respiratory signals using the adaptive filter, and these respiratory signals are correlated with the portal image to predict the tumor motion. A nonlinear dynamic system is reconstructed by the system history based on the previous measurement [98].

The adaptive filter continuously updated the coefficient parameters using least mean square method to predict the respiratory motion, as follows:

$$y(t) = B(q)u(t), \quad (2.15)$$

where $y(t)$ is prediction of the respiratory motion, $B(q)$ is a linear model including the delay operator q with $B(q) = b_0q^0 + b_1q^{-1} + \dots + b_{n-1}q^{-n+1}$, and $u(t)$ is the history information including the past n samples of the infrared camera. In addition, ATTS modeled the correlation between two signals using means of nonlinear methods to determine the tumor position. That means dynamic nonlinear system examines the current indirect signal in the past samples using x (and y)-coordinate motion range (mm), maximum velocity of x (and y)-coordinate (mm/s), and mean cycle period (s) and then the best-fitting direct signals were adapted to predict the tumor motion [68]. Wilbert et al. showed that the maximum standard deviation was 0.8 mm for x -coordinate and 1.0 mm for y -coordinate. However, there are limits in velocity range between 8.5 mm/s (y (and z)-coordinate) and 9.5 mm/s (x -coordinate), so that the amplitude acquired below these limits will not lead to efficient prediction with such a linear model [68].

2.3.3.3 Interacting Multiple Model Filter

An interacting multiple model (IMM) filter can be used as a suboptimal hybrid filter for respiratory motion prediction to combine different filter models with improved control of filter divergence [72, 81, 83]. It makes the overall filter recursive by modifying the initial state vector and covariance of each filter through a probability weighted mixing of all the model states and probabilities, as shown in Fig. 2.15 [81, 83].

Figure 2.15 shows a recursive filter of IMM with a constant velocity (CV) model and a constant acceleration (CA) model, where three steps—interaction,

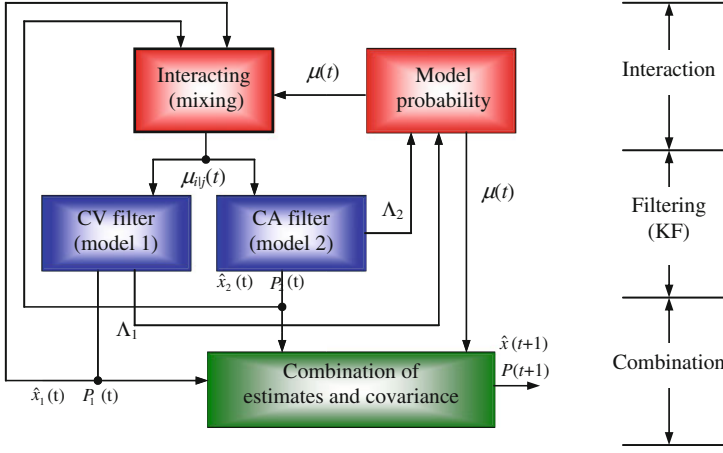


Fig. 2.15 An interactive multiple model for respiratory motion prediction. In the interaction step, model and mixing probabilities are initialized and updated. In the filtering step, the mixed filtering prediction (\hat{x}_i) of target position and the associated covariance (P_i) are updated within each model. In the combination step, the actual prediction of target position is computed for output purposes with the mixing probability

filtering, and combination—are repeated by each time instant t . In the interaction step, model probability ($\mu_j(t)$) and mixing probability ($\mu_{ij}(t)$) are initialized and updated based on a 2×2 Markovian transition matrix (Π) with its component π_{ij} that represents the transition probability from model i to model j , satisfied with $\sum_j \pi_{ij} = 1$ for $i = 1, 2$, as follows [81, 83]:

$$\mu_j(t) = \sum_{i=1}^2 \pi_{ij} \mu_i(t-1), \quad \mu_{ij}(t) = \pi_{ij} \mu_i(t-1) / \mu_j(t), \quad (2.16)$$

where we denote $\mu_j(t)$ as the predicted probability for model j at time step t , and $\mu_{ij}(t)$ as the weight for the conditional transition probability from model i for the previous time step $t-1$ to model j for the current time step t . In the filtering step, the mixed filtering prediction of target position ($\hat{x}_j(t)$) and the associated covariance ($P_j(t)$) are updated with Kalman gain, likelihood update (Λ_j) and model probability ($\mu_j(t)$), shown in Fig. 2.15 [81]. In combination step, the actual prediction of target position, i.e., combination of estimates and covariance, is computed for output purposes with the mixing probability, such as estimation $\hat{x}(t+1) = \sum_j \hat{x}_j(t+1) \mu_j(t)$, and covariance $P(t+1) = \sum_j \{P_j(t) + [\hat{x}_j(t) - \hat{x}(t)] [\hat{x}_j(t) - \hat{x}(t)]^T\} \mu_j(t)$ [83].

Putra et al. showed that the prediction of IMM filter was better than the prediction of the Kalman filters with CV and CA model, and that the errors of the IMM filter were less than 0.98 mm with 200 ms latency [81]. The limitation of this method is that the above hybrid method was proposed for dynamic iteration in one dimensional

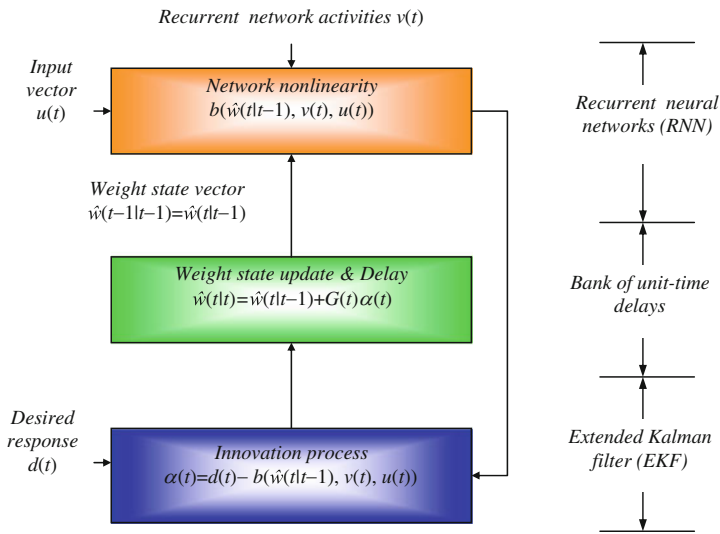


Fig. 2.16 Closed-loop feedback system incorporating EKF for RNN. RNN performs a role of the predictor with network nonlinear function, whereas EKF performs a role of the corrector with innovation process in a recursive manner in this system

prediction, so that independent parallel filters should be implemented for 3D motions [83]. Furthermore, IMM method was investigated to compare with a prediction method based on the first-order extended Kalman filter by Hong et al. [72]. Breathing variation, such as deep or fast breathing, results in a relatively low accuracy of breathing motion prediction. King et al. showed that a multiple sub-model method based on breathing amplitude can provide an adaptive motion model with adjusting basic sub-models [100]. They validated that the combined models with multiple sub-models can show the prediction errors of 1.0–2.8 mm.

2.3.3.4 Hybrid Extended Kalman Filter

Kalman filters are widely used for training nonlinear function of the state estimation and prediction for desired input–output mappings [72, 81, 83]. Kalman filter can also be used for supervised training framework of recurrent neural networks using nonlinear sequential state estimators. The prediction and correction property is an intrinsic property of Kalman filter. In Hybrid extended Kalman filter (HEKF), recurrent neural network (RNN) performs a role of the predictor with network nonlinear function including input vector (u), recurrent network activities (v), and adaptive weight state vectors (w), whereas EKF performs a role of the corrector with innovation process in a recursive manner, as shown in Fig. 2.16 [101, 102].

Table 2.4 Hybrid prediction algorithms of respiratory motion

Methods	Prediction error and evaluation metrics	Features (system)
Adaptive neuro-fuzzy inference system [80]	0.628 mm (coached), 1.798 mm (non-coached), RMSE	25 Hz sample frequency (RPM)
Adaptive tumor tracking system [68]	0.8 mm (x-max), 1.0 mm (y-max), standard deviation	Megavoltage imaging with infrared system (ELEKTA)
Interacting multiple model filter [81]	0.98 mm with 200 ms latency for 5 Hz, RMSE	Kalman CV and CA, Markovian transition (RPM)
Adaptive motion model [100]	1.0–2.8 mm	Standard deviation
Hybrid extended Kalman filter [15]	Less than 0.15 with 200 ms latency, normalized RMSE	26 Hz sample frequency (CyberKnife)

The recurrent network is expressed by the network nonlinearity function $b(\cdot, \cdot, \cdot)$ with input vectors $u(t)$, the internal state of the recurrent network activities $v(t)$, and the weight state vector $\hat{w}(t|t-1)$. The innovation process $\alpha(t)$ of EKF is expressed as follows:

$$\alpha(t) = d(t) - b(\hat{w}(t|t-1), v(t), u(t)). \quad (2.17)$$

where $b(\cdot, \cdot, \cdot)$ is the network nonlinear function of vector-value measurement. The weight state vector is updated with the Kalman gain $G(t)$ and the innovation process [102].

Puskorius et al. proposed a Decoupled EKF (DEKF) as a practical solution for the computational resource management of covariance value with EKF for RNN [101]. Suk et al. applied DEKF to the prediction of respiratory motion. They evaluated that the prediction accuracy of the proposed HEKF and DEKF were less than 0.15 and 0.18 (nRMSE) with 200 ms latency, respectively. They also validated that HEKF can improve the average prediction overshoot more than 60 %, compared with DEKF. This method comprehensively organized the multiple breathing signals with adapting the coupling technique to compensate the computational accuracy, whereas the computational requirements were increased to improve the prediction accuracy [15]. We summarized the prediction accuracy and a representative feature for each method of the hybrid approach, as shown in Table 2.4.

2.4 Open Questions for Prediction of Respiratory Motion

Variable open questions on the prediction of respiratory motion are still remained to be solved in a foreseeable future. In this chapter, we will point out general open questions for the advanced radiotherapy technology, but open issues are not limited to the following issues described in this study.

2.4.1 Changes of Respiratory Patterns

The respiratory patterns identified in the treatment preparation may be changed before or during the treatment delivery. A real-time tracking method may compensate for changes of respiratory pattern during treatment delivery, but this method can be interrupted by other parameters, e.g., cardiac and gastrointestinal motion, baseline shifts, tumor deformation, highly fluctuating amplitudes of respiratory motion, and so on [26]. Therefore, it requires clinical solutions to adjust or construct changes of respiratory patterns.

2.4.2 Tumor Deformation and Target Dosimetry

Lung deformation derived from respiration may change tumor shapes, or a tumor may change its own shape by itself [103]. Some studies investigated that irregular breathing patterns required more extended clinical target volume compared with regular breathing patterns [94]. Sophisticated target dosimetry based on tumor deformation also should be considered for the optimized treatment delivery.

2.4.3 Irregular Pattern Detection

A real-time tumor-tracking method, where the prediction of irregularities really becomes relevant [79], has yet to be clinically established. In the thoracic radiotherapy, other parameters including cardiac and gastrointestinal motion can affect the prediction of respiratory patterns. Respiratory patterns of some patients may have dramatically irregular motions of peaks and valleys position, compared with others [104]. It requires a new strategy or standard for irregular breathing classification depending on a degree of breathing irregularity for each patient. Irregular pattern detection may be used to adjust a margin value, e.g., the patients assigned with regular patterns would be dealt with tight margins to prevent health tissues from irradiating by high-dose treatment. For the patients assigned with irregular patterns, safety margins should be determined by patient-specific irregularity to compensate for the baseline shifts or highly fluctuating amplitudes that are not covered by standard safety margins [94, 105].

2.5 Summary

In this chapter, we have showed current radiotherapy technologies including tools for measuring target position during radiotherapy and tracking-based delivery systems including Linacs, MLC, and robotic couch. We have also explained three

prediction approaches including *model-based*, *model-free*, and *hybrid* prediction algorithms. In the previous chapter, we have described some questions that still remain to be solved in the future, exemplified by changes of respiratory patterns, tumor deformation target dosimetry, and irregular pattern detection. Open questions are not limited to the issues described in the study.

References

1. <http://www.cancer.gov/cancertopics/coping/radiation-therapy-and-you/>
2. C. Ozhasoglu, M.J. Murphy, Issues in respiratory motion compensation during external-beam radiotherapy. *Int. J. Radiat. Oncol. Biol. Phys.* **52**(5), 1389–1399 (2002)
3. L. Walsh, M. Morgia, A. Fyles, M. Milosevic, Technological advances in radiotherapy for cervical cancer. *Curr. Opin. Oncol.* **23**(5), 512–518 (2011)
4. L.I. Cervino, Y. Jiang, A. Sandhu, S.B. Jiang, Tumor motion prediction with the diaphragm as a surrogate: a feasibility study. *Phys. Med. Biol.* **55**(9), 221–229 (2010)
5. Q. Zhang, A. Pevsner, A. Hertanto, Y. Hu, K.E. Rosenzweig, C.C. Ling, G.S. Mageras, A patient-specific respiratory model of anatomical motion for radiation treatment planning. *Med. Phys.* **34**(12), 4772–4781 (2007)
6. K. Nakagawa, K. Yoda, Y. Masutani, K. Sasaki, K. Ohtomo, A rod matrix compensator for small-field intensity modulated radiation therapy: a preliminary phantom study. *IEEE Trans. Biomed. Eng.* **54**(5), 943–946 (2007)
7. R. Lu, R.J. Radke, L. Hong, C. Chui, J. Xiong, E. Yorke, A. Jackson, Learning the relationship between patient geometry and beam intensity in breast intensity-modulated radiotherapy. *IEEE Trans. Biomed. Eng.* **53**(5), 908–920 (2006)
8. M. Schwarz, J.V.D. Geer, M.V. Herk, J.V. Lebesque, B.J. Mijnheer, E.M.F. Damen, Impact of geometrical uncertainties on 3D CRT and IMRT dose distributions for lung cancer treatment. *Int. J. Radiat. Oncol. Biol. Phys.* **65**(4), 1260–1269 (2006)
9. T. Depuydt, D. Verellen, O. Haas, T. Gevaert, N. Linthout, M. Duchateau, K. Tournel, T. Reynders, K. Leysen, M. Hoogeman, G. Storme, M. De Ridder, Geometric accuracy of a novel gimbals based radiation therapy tumor tracking system. *Radiother. Oncol.* **98**(3), 365–372 (2011)
10. I. Buzurovic, K. Huang, Y. Yu, T.K. Podder, A robotic approach to 4D real-time tumor tracking for radiotherapy. *Phys. Med. Biol.* **56**(5), 1299–1318 (2011)
11. J.R. Wong, L. Grimm, M. Uematsu, R. Oren, C.W. Cheng, S. Merrick, P. Schiff, Image-guided radiotherapy for prostate cancer by CT-linear accelerator combination: prostate movements and dosimetric considerations. *Int. J. Radiat. Oncol. Biol. Phys.* **61**(2), 561–569 (2005)
12. A. Sawant, R.L. Smith, R.B. Venkat, L. Santanam, B. Cho, P. Poulsen, H. Cattell, L.J. Newell, P. Parikh, P.J. Keall, Toward submillimeter accuracy in the management of intrafraction motion: the integration of real-time internal position monitoring and multileaf collimator target tracking. *Int. J. Radiat. Oncol. Biol. Phys.* **74**(2), 575–582 (2009)
13. H. Liu, Q. Wu, Dosimetric and geometric evaluation of a hybrid strategy of offline adaptive planning and online image guidance for prostate cancer radiotherapy. *Phys. Med. Biol.* **56**(15), 5045–5062 (2011)
14. C. Ling, P. Zhang, T. Etmektzoglou, J. Star-Lack, M. Sun, E. Shapiro, M. Hunt, Acquisition of MV-scatter-free kilovoltage CBCT images during RapidArcTM or VMAT. *Radiother. Oncol.* **100**(1), 145–149 (2011)
15. S.J. Lee, Y. Motai, M. Murphy, Respiratory motion estimation with hybrid implementation of extended Kalman filter. *IEEE Trans. Ind. Electron.* **59**(11), 4421–4432 (2012)

16. R. Zeng, J.A. Fessler, J.M. Balter, Estimating 3D respiratory motion from orbiting views by tomographic image registration. *IEEE Trans. Med. Imaging* **26**(2), 153–163 (2007)
17. W. Bai, S.M. Brady, Motion correction and attenuation correction for respiratory gated PET images. *IEEE Trans. Med. Imaging* **30**(2), 351–365 (2011)
18. D. Sarrut, B. Delhay, P. Villard, V. Boldea, M. Beuve, P. Clarysse, A comparison framework for breathing motion estimation methods from 4D imaging. *IEEE Trans. Med. Imaging* **26**(12), 1636–1648 (2007)
19. J. Ehrhardt, R. Werner, A. Schmidt-Richberg, H. Handels, Statistical modeling of 4D respiratory lung motion using diffeomorphic image registration. *IEEE Trans. Med. Imaging* **30**(2), 251–265 (2011)
20. G.S. Stamatakis, D.D. Dionysiou, E.I. Zacharaki, N.A. Mouravliansky, K.S. Nikita, N.K. Uzunoglu, In silico radiation oncology: combining novel simulation algorithms with current visualization techniques. *Proc. IEEE* **90**(11), 1764–1777 (2002)
21. S.J. McQuaid, T. Lambrou, V.J. Cunningham, V. Bettinardi, M.C. Gilardi, B.F. Hutton, The application of a statistical shape model to diaphragm tracking in respiratory-gated cardiac PET images. *Proc. IEEE* **97**(12), 2039–2052 (2009)
22. H. Zaidi, B.M.W. Tsui, Review of computational anthropomorphic anatomical and physiological models. *Proc. IEEE* **97**(12), 1938–1953 (2009)
23. M. Niedre, V. Ntziachristos, Elucidating structure and function in vivo with hybrid fluorescence and magnetic resonance imaging. *Proc. IEEE* **96**(3), 382–396 (2008)
24. J. He, G.J. O’Keefe, S.J. Gong, G. Jones, T. Saunderson, A.M. Scott, M. Geso, A novel method for respiratory motion gated with geometric sensitivity of the scanner in 3D PET. *IEEE Trans. Nucl. Sci.* **55**(5), 2557–2565 (2008)
25. H. Tadayyon, A. Lasso, A. Kaushal, P. Guion, G. Fichtinger, Target motion tracking in MRI-guided transrectal robotic prostate biopsy. *IEEE Trans. Biomed. Eng.* **58**(11), 3135–3142 (2011)
26. P.J. Keall, G.S. Mageras, J.M. Balter, R.S. Emery, K.M. Forster, S.B. Jiang, J.M. Kapatoes, D.A. Low, M.J. Murphy, B.R. Murray, C.R. Ramsey, M.B. Van Herk, S.S. Vedam, J.W. Wong, E. Yorke, The management of respiratory motion in radiation oncology report of AAPM Task Group 76. *Med. Phys.* **33**(10), 3874–3900 (2006)
27. A. Filler, The history, development and impact of computed imaging in neurological diagnosis and neurosurgery: CT, MRI, and DTI. *Internet J. Neurosurg.* **7**(1), 1–69 (2009)
28. M.J. Murphy, Tracking moving organs in real time. *Semin. Radiat. Oncol.* **14**(1), 91–100 (2004)
29. R.I. Berbeco, S. Nishioka, H. Shirato, G.T.Y. Chen, S.B. Jiang, Residual motion of lung tumours in gated radiotherapy with external respiratory surrogates. *Phys. Med. Biol.* **50**(16), 3655–3667 (2005)
30. X. Tang, G.C. Sharp, S.B. Jiang, Fluoroscopic tracking of multiple implanted fiducial markers using multiple object tracking. *Phys. Med. Biol.* **52**(14), 4081–4098 (2007)
31. S.B. Jiang, Radiotherapy of mobile tumors. *Semin. Radiat. Oncol.* **16**(4), 239–248 (2006)
32. C. Shi, N. Papanikolaou, Tracking versus gating in the treatment of moving targets. *Eur. Oncol. Dis.* **1**(1), pp. 83–86 (2007)
33. R.D. Wiersma, W. Mao, L. Xing, Combined kV and MV imaging for real-time tracking of implanted fiducial markers. *Med. Phys.* **35**(4), 1191–1198 (2008)
34. P.J. Keall, A.D. Todor, S.S. Vedam, C.L. Bartee, J.V. Siebers, V.R. Kini, R. Mohan, On the use of EPID-based implanted marker tracking for 4D radiotherapy. *Med. Phys.* **31**(12), 3492–3499 (2004)
35. A. Schweikard, H. Shiomi, J. Adler, Respiration tracking in radiosurgery. *Med. Phys.* **31**(10), 2738–2741 (2004)
36. <https://rpop.iaea.org>
37. K.M. Langen, D.T.L. Jones, Organ motion and its management. *Int. J. Radiat. Oncol. Biol. Phys.* **50**(1), 265–278 (2001)
38. R. Werner, J. Ehrhardt, R. Schmidt, H. Handels, Patient-specific finite element modeling of respiratory lung motion using 4D CT image data. *Med. Phys.* **36**(5), 1500–1510 (2009)

39. D. Yang, W. Lu, D.A. Low, J.O. Deasy, A.J. Hope, I. El Naqa, 4D-CT motion estimation using deformable image registration and 5D respiratory motion modeling. *Med. Phys.* **35**(10), 4577–4590 (2008)
40. A.A. Patel, J.A. Wolfgang, A. Niemierko, T.S. Hong, T. Yock, N.C. Choi, Implications of respiratory motion as measured by four-dimensional computed tomography for radiation treatment planning of esophageal cancer. *Int. J. Radiat. Oncol. Biol. Phys.* **74**(1), 290–296 (2009)
41. T.O.J. Fuchs, M. Kachelriess, W.A. Kalender, Fast volume scanning approaches by X-ray-computed tomography. *Proc. IEEE* **91**(10), 1492–1502 (2003)
42. S.R. Cherry, A.Y. Louie, R.E. Jacobs, The integration of positron emission tomography with magnetic resonance imaging. *Proc. IEEE* **96**(3), 416–438 (2008)
43. A.P. Dhawan, B. D'Alessandro, X. Fu, Optical imaging modalities for biomedical applications. *IEEE Rev. Biomed. Eng.* **3**, 69–92 (2010)
44. A.P. Gibson, J.C. Hebden, S.R. Arridge, Recent advances in diffuse optical imaging. *Phys. Med. Biol.* **50**(4), R1–R43 (2005)
45. Y.K. Park, S. Kim, H. Kim, I.H. Kim, K. Lee, S.J. Ye, Quasi-breath-hold technique using personalized audio-visual biofeedback for respiratory motion management in radiotherapy. *Med. Phys.* **38**(6), 3114–3124 (2011)
46. A. Schweikard, G. Glosser, M. Bodduluri, M.J. Murphy, J.R. Adler, Robotic motion compensation for respiratory movement during radiosurgery. *Comput. Aided Surg.* **5**(4), 263–277 (2000)
47. W.D. D'Souza, S.A. Naqvi, C.X. Yu, Real-time intra-fraction-motion tracking using the treatment couch: a feasibility study. *Phys. Med. Biol.* **50**(17), 4021–4033 (2005)
48. I. Buzurovic, T.K. Podder, K. Huang, Y. Yu, Tumor motion prediction and tracking in adaptive radiotherapy. *IEEE International Conference on Bioinformatics and Bioengineering*, (2010). pp. 273–278
49. L. Brewster, R. Mohan, G. Mageras, C. Burman, S. Leibel, Z. Fuks, Three dimensional conformal treatment planning with multileaf collimators. *Int. J. Radiat. Oncol. Biol. Phys.* **33**(5), 1081–1089 (1995)
50. S. Han-Oh, B.Y. Yi, F. Lerma, B.L. Berman, M. Gui, C. Yu, Verification of MLC based real-time tumor tracking using an electronic portal imaging device. *Med. Phys.* **37**(6), 2435–2440 (2010)
51. B.Y. Yi, S. Han-Oh, F. Lerma, B.L. Berman, C. Yu, Real-time tumor tracking with preprogrammed dynamic multileaf-collimator motion and adaptive dose-rate regulation. *Med. Phys.* **35**(9), 3955–3962 (2008)
52. T. Gevaert, D. Verellen, B. Engels, T. Depuydt, K. Heuninckx, K. Tournel, M. Duchateau, T. Reynders, M. De Ridder, Clinical evaluation of a robotic 6-degree of freedom treatment couch for frameless radiosurgery. *Int. J. Radiat. Oncol. Biol. Phys.* **83**(1), 467–474 (2012)
53. <http://www.morsecyberknife.com/CyberKnife-System>
54. E.W. Pepin, H. Wu, Y. Zhang, B. Lord, Correlation and prediction uncertainties in the CyberKnife Synchrony respiratory tracking system. *Med. Phys.* **38**(7), 4036–4044 (2011)
55. D. Ruan, P. Keall, Online prediction of respiratory motion: multidimensional processing with low-dimensional feature learning. *Phys. Med. Biol.* **55**(11), 3011–3025 (2010)
56. N. Riaz, P. Shanker, R. Wiersma, O. Gudmundsson, W. Mao, B. Widrow, L. Xing, Predicting respiratory tumor motion with multi-dimensional adaptive filters and support vector regression. *Phys. Med. Biol.* **54**(19), 5735–5748 (2009)
57. M.J. Murphy, S. Dieterich, Comparative performance of linear and nonlinear neural networks to predict irregular breathing. *Phys. Med. Biol.* **51**(22), 5903–5914 (2006)
58. D. Ruan, Prospective detection of large prediction errors: a hypothesis testing approach. *Phys. Med. Biol.* **55**(13), 3885–3904 (2010)
59. P.R. Poulsen, B. Cho, D. Ruan, A. Sawant, P.J. Keall, Dynamic multileaf collimator tracking of respiratory target motion based on a single kilovoltage imager during arc radiotherapy. *Int. J. Radiat. Oncol. Biol. Phys.* **77**(2), 600–607 (2010)

60. G. Tchoupo, A. Docef, Nonlinear set membership time series prediction of breathing. *European Signal Processing Conference* (2008)
61. W.D. D'Souza, K. Malinowski, H.H. Zhang, Machine learning for intra-fraction tumor motion modeling with respiratory surrogates. *International Conference on Machine Learning and Applications* (2009). pp. 463–467
62. <http://medicalphysicsweb.org/cws/companies/category/165>
63. http://www.varian.com/us/oncology/radiation_oncology/
64. S.S. Vedam, V.R. Kini, P.J. Keall, V. Ramakrishnan, H. Mostafavi, R. Mohan, Quantifying the predictability of diaphragm motion during respiration with a noninvasive external marker. *Med. Phys.* **30**(4), 505–513 (2003)
65. H. Shirato, S. Shimizu, T. Kunieda, K. Kitamura, M. van Herk, K. Kagei, T. Nishioka, S. Hashimoto, K. Fujita, H. Aoyama, K. Tsuchiya, K. Kudo, K. Miyasaka, Physical aspects of a real-time tumor-tracking system for gated radiotherapy. *Int. J. Radiat. Oncol. Biol. Phys.* **48**(4), 1187–1195 (2000)
66. H. Shirato, S. Shimizu, K. Kitamura, T. Nishioka, K. Kagei, S. Hashimoto, H. Aoyama, T. Kunieda, N. Shinohara, H. Dosaka-Akita, K. Miyasaka, Four-dimensional treatment planning and fluoroscopic real-time tumor tracking radiotherapy for moving tumor. *Int. J. Radiat. Oncol. Biol. Phys.* **48**(2), 435–442 (2000)
67. T. Harada, H. Shirato, S. Ogura, S. Oizumi, K. Yamazaki, S. Shimizu, R. Onimaru, K. Miyasaka, M. Nishimura, H. Dosaka-Akita, Real-time tumor-tracking radiation therapy for lung carcinoma by the aid of insertion of a gold marker using bronchofiberscopy. *Cancer* **95**(8), 1720–1727 (2002)
68. J. Wilbert, J. Meyer, K. Baier, M. Guckenberger, C. Herrmann, R. Hess, C. Janka, L. Ma, T. Mersebach, A. Richter, M. Roth, K. Schilling, M. Flentje, Tumor tracking and motion compensation with an adaptive tumor tracking system (ATTS): system description and prototype testing. *Med. Phys.* **35**(9), 3911–3921 (2008)
69. http://www.elekta.com/healthcare_international_elekta_oncology.php
70. <http://www.medical.siemens.com>
71. J.E. Bayouth, Siemens multileaf collimator characterization and quality assurance approaches for intensity-modulated radiotherapy. *Int. J. Radiat. Oncol. Biol. Phys.* **71**(1), S93–S97 (2008)
72. S.-M. Hong, B.-H. Jung, D. Ruan, Real-time prediction of respiratory motion based on a local dynamic model in an augmented space. *Phys. Med. Biol.* **56**(6), 1775–1789 (2011)
73. A. Kalet, G. Sandison, H. Wu, R. Schmitz, A state-based probabilistic model for tumor respiratory motion prediction. *Phys. Med. Biol.* **55**(24), 7615–7631 (2010)
74. S.S. Vedam, P.J. Keall, A. Docef, D.A. Todor, V.R. Kini, R. Mohan, Predicting respiratory motion for four-dimensional radiotherapy. *Med. Phys.* **31**(8), 2274–2283 (2004)
75. G.C. Sharp, S.B. Jiang, S. Shimizu, H. Shirato, Prediction of respiratory tumour motion for real-time image-guided radiotherapy. *Phys. Med. Biol.* **49**, 425–440 (2004)
76. Q. Ren, S. Nishioka, H. Shirato, R.I. Berbeco, Adaptive prediction of respiratory motion for motion compensation radiotherapy. *Phys. Med. Biol.* **52**(22), 6651–6661 (2007)
77. K.C. McCall, R. Jeraj, Dual-component model of respiratory motion based on the periodic autoregressive moving average (periodic ARMA) method. *Phys. Med. Biol.* **52**(12), 3455–3466 (2007)
78. H. Wu, G.C. Sharp, B. Salzberg, D. Kaeli, H. Shirato, S.B. Jiang, A finite state model for respiratory motion analysis in image guided radiation therapy. *Phys. Med. Biol.* **49**(23), 5357–5372 (2004)
79. M.J. Murphy, D. Pikhrel, Optimization of an adaptive neural network to predict breathing. *Med. Phys.* **36**(1), 40–47 (2009)
80. M. Kakar, H. Nyström, L.R. Aarup, T.J. Nøttrup, D.R. Olsen, Respiratory motion prediction by using the adaptive neuro fuzzy inference system (ANFIS). *Phys. Med. Biol.* **50**(19), 4721–4728 (2005)

81. D. Putra, O.C. L. Haas, J.A. Mills, K. J. Bumham, Prediction of tumour motion using interacting multiple model filter. *International Conference on Advances in Medical, Signal and Information Processing* (2006). pp. 1–4
82. P.S. Verma, H. Wu, M.P. Langer, I.J. Das, G. Sandison, Survey: real-time tumor motion prediction for image guided radiation treatment. *Comput. Sci. Eng.* **13**(5), 24–35 (2011)
83. D. Putra, O.C.L. Haas, J.A. Mills, K.J. Burnham, A multiple model approach to respiratory motion prediction for real-time IGRT. *Phys. Med. Biol.* **53**(6), 1651–1663 (2008)
84. F. Wang, V. Balakrishnan, Robust steady-state filtering for systems with deterministic and stochastic uncertainties. *IEEE Trans. Sig. Process.* **51**(10), 2550–2558 (2003)
85. F. Ernst, A. Schweikard, Forecasting respiratory motion with accurate online support vector regression (SVRpred). *Int. J. Comput. Assist. Radiol. Surg.* **4**(5), 439–447 (2009)
86. H. Drucker, C.J.C. Burges, L. Kaufman, A. Smola, V. Vapnik, Support vector regression machines. *Adv. Neural Inf. Process. Syst.* **9**, 155–161 (1996)
87. S. Chen, S. Zhou, F.F. Yin, L.B. Marks, S.K. Das, Investigation of the support vector machine algorithm to predict lung radiation-induced pneumonitis. *Med. Phys.* **34**(10), 3808–3814 (2007)
88. L.I. Cerviño, A.K.Y. Chao, A. Sandhu, S.B. Jiang, The diaphragm as an anatomic surrogate for lung tumor motion. *Phys. Med. Biol.* **54**(11), 3529–3541 (2009)
89. F.O. Spoelstra, J.R. van Sörnsen de Koste, A. Vincent, J.P. Cuijpers, B.J. Slotman, S. Senan, An evaluation of two internal surrogates for determining the three-dimensional position of peripheral lung tumors. *Int. J. Radiat. Oncol. Biol. Phys.* **74**(2), 623–629 (2009)
90. D. Ruan, J.A. Fessler, J.M. Balter, Real-time prediction of respiratory motion based on local regression methods. *Phys. Med. Biol.* **52**(23), 7137–7152 (2007)
91. J.G. Parker, B.A. Mair, D.R. Gilland, Respiratory motion correction in gated cardiac SPECT using quaternion-based, rigid-body registration. *Med. Phys.* **36**(10), 4742–4754 (2009)
92. D.A. Low, P.J. Parikh, W. Lu, J.F. Dempsey, S.H. Wahab, J.P. Hubenschmidt, M.M. Nystrom, M. Handoko, J.D. Bradley, Novel breathing motion model for radiotherapy. *Int. J. Radiat. Oncol. Biol. Phys.* **63**(3), 921–929 (2005)
93. M. Isaksson, J. Jaldén, M.J. Murphy, On using an adaptive neural network to predict lung tumor motion during respiration for radiotherapy applications. *Med. Phys.* **32**(12), 3801–3809 (2005)
94. Y.D. Mutfaf, C.J. Scicutella, D. Michalski, K. Fallon, E.D. Brandner, G. Bednarz, M.S. Huq, A simulation study of irregular respiratory motion and its dosimetric impact on lung tumors. *Phys. Med. Biol.* **56**(3), 845–859 (2011)
95. S. Vedam, A. Docef, M. Fix, M. Murphy, P. Keall, Dosimetric impact of geometric errors due to respiratory motion prediction on dynamic multileaf collimator-based four-dimensional radiation delivery. *Med. Phys.* **32**(6), 1607–1620 (2005)
96. S. Haykin, *Adaptive Filter Theory*, 3rd ed. (Prentice Hall, Englewood Cliffs, 1996)
97. C.C. Lee, Fuzzy logic in control systems: fuzzy logic controller. *IEEE Trans. Syst. Man Cybern.* **20**(2), 404–418 (1990)
98. L. Ma, C. Herrmann, K. Schilling, Modeling and prediction of lung tumor motion for robotic assisted radiotherapy. *IEEE/RSJ International Conference on Intelligent Robots and Systems* (2007). pp. 189–194
99. J. Meyer, A. Richter, K. Baier, J. Wilbert, M. Guckenberger, M. Flentje, Tracking moving objects with megavoltage portal imaging: a feasibility study. *Med. Phys.* **33**(5), 1275–1280 (2006)
100. A.P. King, K.S. Rhode, R.S. Razavi, T.R. Schaeffter, An adaptive and predictive respiratory motion model for image-guided interventions: theory and first clinical application. *IEEE Trans. Med. Imaging* **28**(12), 2020–2032 (2009)
101. G.V. Puskorius, L.A. Feldkamp, Neurocontrol of nonlinear dynamical systems with Kalman filter trained recurrent networks. *IEEE Trans. Neural Netw.* **5**(2), 279–297 (1994)
102. S. Haykin, *Neural Networks and Learning Machines*, 3rd edn. (Pearson, London, 2009)
103. B. Guo, X.G. Xu, C. Shi, Real time 4D IMRT treatment planning based on a dynamic virtual patient model: proof of concept. *Med. Phys.* **38**(5), 2639–2650 (2011)

104. W. Lu, M.M. Nystrom, P.J. Parikh, D.R. Fooshee, J.P. Hubenschmidt, J.D. Bradley, D.A. Low, A semi-automatic method for peak and valley detection in free-breathing respiratory waveforms. *Med. Phys.* **33**(10), 3634–3636 (2006)
105. L. Huang, K. Park, T. Boike, P. Lee, L. Papiez, T. Solberg, C. Ding, R.D. Timmerman, A study on the dosimetric accuracy of treatment planning for stereotactic body radiation therapy of lung cancer using average and maximum intensity projection images. *Radiother. Oncol.* **96**(1), 48–54 (2010)

Prediction and Classification of Respiratory Motion

Lee, S.J.; Motai, Y.

2014, IX, 167 p. 67 illus., 65 illus. in color., Hardcover

ISBN: 978-3-642-41508-1